

Research Article

Full-Field Strain Characterizations and Fracture Process of Rock Blasting Using a Small-Scale Double-Hole Bench Model

Jun Yang,¹ Xin Liu ,¹ Zhenyang Xu,² Hongliang Tang,¹ and Qi Yu³

¹State Key Laboratory of Explosion Science and Technology, Beijing Institute of Technology, Beijing 100081, China

²School of Mining Engineering, University of Science and Technology Liaoning, Liaoning Anshan 114051, China

³China Ordnance Industry Fire and Explosives Engineering and Safety Technology Research Institute, China North Industries Group Corporation Limited, Beijing 100053, China

Correspondence should be addressed to Xin Liu; xinliu0412@foxmail.com

Received 27 December 2019; Revised 8 August 2020; Accepted 17 August 2020; Published 28 August 2020

Academic Editor: Rafael J. Bergillos

Copyright © 2020 Jun Yang et al. This is an open access article distributed under the Creative Commons Attribution License, which permits unrestricted use, distribution, and reproduction in any medium, provided the original work is properly cited.

A small-scale double-hole bench model is designed with granite to study the fracture mechanism of rock blasting. By combining high-speed camera and digital image correlation, the full-field strain characterization and fracture process of the specimen bevel surface are investigated. The preliminary test results show that the strain concentration zone corresponds to the crack propagation location, and digital image correlation can well detect the crack propagation. In addition, through observing the crack propagation pattern on the specimen bevel surface, it can be seen that the fracture of the specimen is caused by the dominant horizontal crack and the dominant vertical crack, and the generation of the dominant horizontal crack takes precedence over that of the dominant vertical. Finally, the measurements of two-dimensional digital image correlation and three-dimensional digital image correlation are discussed.

1. Introduction

As the main means of rock excavation in the fields of mining production, water conservancy and hydropower, transportation, and infrastructure construction, blasting plays an important role in national economic construction, especially in the excavation and blasting of hard rock. How to control rock fragmentation in open-pit blasting is the key point to improve blasting quality at present. With the wide application of digital electronic detonators and hole-by-hole initiation technology in open-pit mining, the reasonable distribution of blasting fragmentation by means of precise time-delay technology has become a hot topic in blasting technology research. The upgrade of blasting equipment promotes the development of blasting technology, and the original blasting theory and its design concept can no longer meet the application needs of new blasting equipment, which inevitably promotes the new development of blasting theory. For a long time, the mechanism of single-hole blasting is studied in many ways, such as blasting action

mechanism partition, blasting stress wave action or blasting gas action, a number of radial cracks, boundary conditions, and so on [1, 2]. The study of single-hole blasting is the foundation. However, field blasting is the result of multihole interaction. Therefore, the investigations of full-field strain characterization and fracture process of rock blasting with double-hole also make sense.

The laboratory-scale model test is one of the main methods to study the blasting fracture mechanism. An investigation of the role of stress waves and quasistatic gas pressure on rock fragmentation was conducted by small-scale blasting in bench shaped blocks of cement-mortar and also of granite. The results showed that the fragmentation obtained is better under the combined action of stress waves and quasistatic gas pressure. From a comparison between the experimental results and the analytical studies, Bhandari [3] concluded that radiating cracks follow the principal stress trajectories. In order to understand the effect of the shock wave and gas pressure on the crack length, Olsson et al. [4] used granite blocks with tow borehole and the

borehole is pretreated; they concluded that the shock wave plays a major role on the crack length in the remaining rock walls and the gases have no significant effect on the crack for an emulsion explosive. Stagg [5] designed a concrete bench model with a scaled-down geometric dimension of 10%, from the dynamic strain and pressure measurements of improved fragmentation tests; he indicated that it may be the result of the interaction between the strain caused by the stress wave and the strain caused by the gas pressure generated by the early explosion hole. By using magnetic mortar blocks with two rows and ten boreholes, Johansson [6] investigated the effect of delay time on blasting fragmentation. The results showed that stress wave interaction has no significant effect on improving blasting fragmentation.

In terms of measurement techniques and methods, two-dimensional digital image correlation (2D-DIC) and three-dimensional digital image correlation (3D-DIC) are already common in investigating rock dynamic response. Gao et al. [7] used a notched semicircular bend (NSCB) specimen to study the rock dynamic fracture process, related information about the fracture process was extracted from the 2D-DIC results. By comparison of the strain gauges and 2D-DIC measurements, Zhang and Zhao [8] concluded that the DIC technique can reliably be used to measure the surface characteristics of rock specimens under dynamic loading. The sandstone dynamic compression was studied by 3D-DIC, and the comparison between 2D-DIC and 3D-DIC was also discussed. Xing et al. [9] concluded that 3D-DIC is better than strain gauge for the actual strain measurements, especially after the peak stress. Using 3D-DIC on granite cubes with single-hole and double-hole under blast loading, He and Yang [10] studied the full-strain field and crack development process.

From the existing research, multiple free surface double-hole bench model based on 3D-DIC under blast loading has not been reported. In this paper, the granite double-hole bench model with multiple free surfaces is designed, two charge diameters are used with the same charge length in the two tests, and the explosives in two boreholes are detonated simultaneously. Full-field strain characterizations of the bench bevel surface are measured by 2D-DIC and 3D-DIC; the fracture process of the double-hole bench model is also investigated.

2. Materials and Methods

Wulian Flower Granite (G3761) is selected from Shandong province for this study. Based on the International Society for Rock Mechanics (ISRM) standards, cylindrical specimens for uniaxial static compressive strength tests (50 × 100 mm) and static tensile strength tests (50 × 25 mm) are cored on the same rock block without obvious joint surface, the quasistatic properties of granite are tested by the hydraulic screen-display universal testing machine (WEP-600), and five replicate tests are performed for each property (Table 1).

The benches usually have two free surfaces in the practice of open bench blasting, and in order to be able to match with the actual situation and have a certain reference and guiding

significance to the site blasting, a double-hole bench model is designed (Figure 1(a)). The double-hole bench specimens are cut into two bevels and a platform by professional rock cutting tools from a granite cuboids with 667 × 509 × 400 mm. The angle between the bevel and the horizontal plane is 70°; this angle is the same as the slope angle of open-pit mining in China. Considering the perpendicularity of the borehole, the boreholes are drilled vertically with 16 mm in diameter by a professional rock drilling tool. The drilled burden is all 60 mm, the borehole spacing is 120 mm, the distance between the second borehole and the boundary is all 240 mm, and the angle between the two free surface boundaries located at the working place is 120°.

Using a homemade positioning device to ensure even packing, the boreholes are filled with high strength fast solidification grouting material (LEISHIBROTHERS® CGM H80) (Figure 1(b)). The use of a homemade positioning device can be guaranteed that the stemming length is 100 mm and the borehole diameter changes to 10 mm, and the effective charge length is 240 mm. The specimens are assembled by means of a self-made jig device (Figure 1(c)). The rules of assembling are to ensure that the specimen fits the rubber and the rubber fits the steel plate. The thickness of the steel plate is 20 mm, the thickness of the rubber is 10 mm, and the diameter of the bolt is 16 mm.

The charging mode is chosen as a radial decoupling charge, RDX is chosen as charging, and two charge diameters are used in this paper (Table 2). The length of the steel tube is 100 mm; i.e., the steel tube extends out 40 mm from the bottom of the borehole. As shown in Figure 1(a), the borehole wall fits the rubber ring and the rubber ring fits the steel tube; the purpose is to guarantee that the RDX in the steel tube with 60 mm in length does not act on the specimen; i.e., the charge length acted on the specimen is 240 mm. The same length of detonating cords is detonated by a detonator, and thus the explosive in the two boreholes are detonated simultaneously.

As shown in Figure 2, the experimental high-speed digital image correlation (DIC) system is set up in the State Key Laboratory of Explosion Science and Technology at the Beijing Institute of Technology (Beijing), the main components of this experimental system are high-speed camera (Photron Fastcam SA5), VIC-2D analysis software, VIC-3D analysis software, the lighting system (Godox SL-200W), and synchronous trigger system. In this paper, the texture of the granite itself is chosen as a speckle pattern. For test 1, the distance between the camera and the specimen is 2.5 m; for test 2, the distance between the two cameras and the specimen is 2.5 m, the shooting angle of the two cameras is 20°, and calibration of the stereovision system is performed using 28 images of a translated and rotated planar dot pattern with a spacing of 12 mm (12 × 9–12.0 mm) [11, 12]. When the detonator detonates, a square signal transmits to the synchronous system, and thus the signal triggers cameras.

The camera shooting parameters for test 1 are as follows. The photograph frames are set as 20000 fps, the image resolution is set as 704 pixels × 520 pixels, and the shooting

TABLE 1: Parameters of granite.

| Density (kg/m ³) | Elastic modulus (GPa) | Poisson ratio | Static compressive strength (MPa) | Static tensile strength (MPa) | P-wave velocity (m/s) |
|------------------------------|-----------------------|---------------|-----------------------------------|-------------------------------|-----------------------|
| 2578 | 35.43 | 0.15 | 70.65 | 3.26 | 4386 |

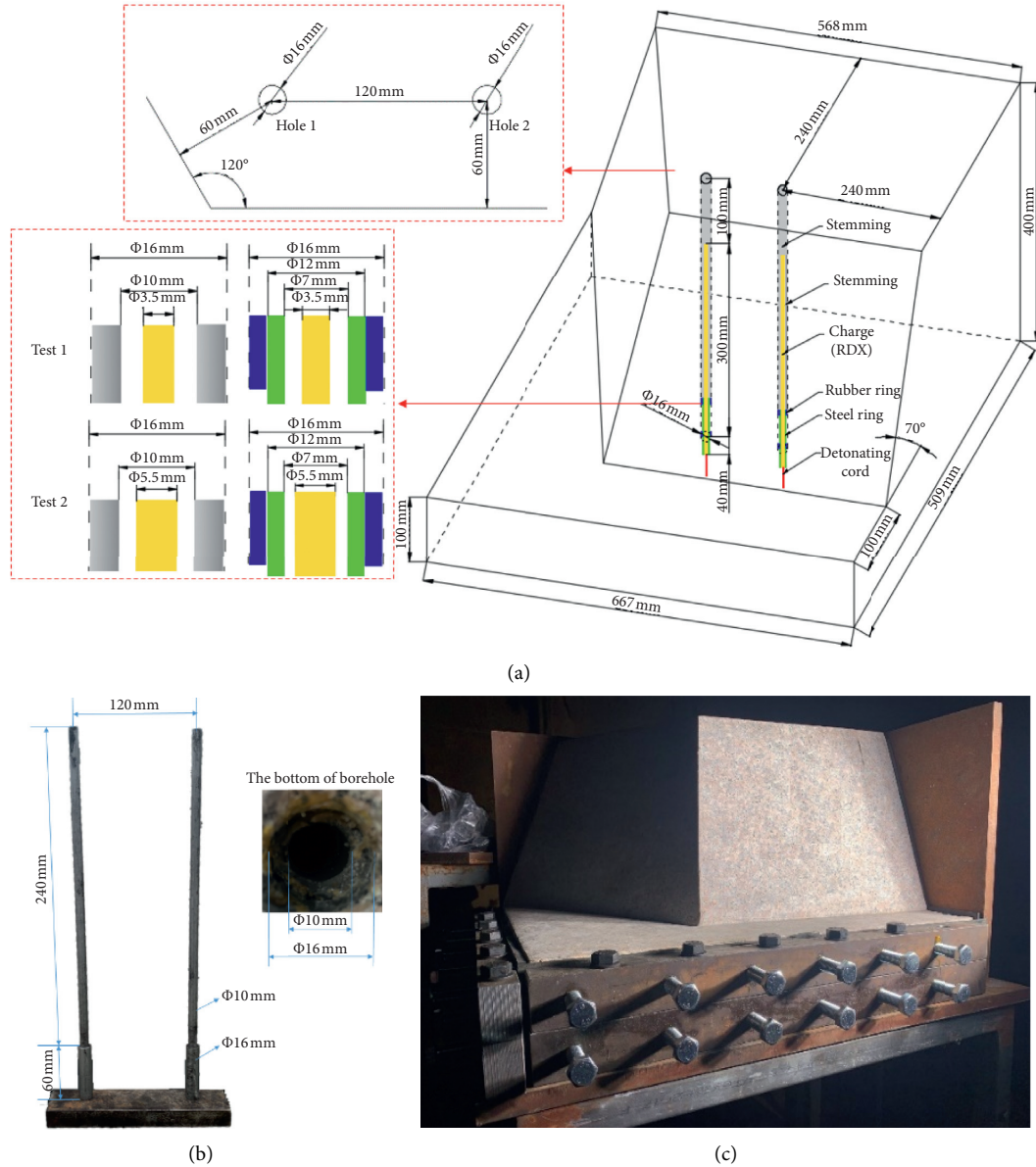


FIGURE 1: Introduction of blasting experiments: (a) details of the specimens; (b) borehole stemming method; (c) specimen restraint.

TABLE 2: Parameters of tests.

| Test no. | Charge length (mm) | Charge diameter (mm) | Charge weight of hole 1 (g) | Charge weight of hole 2 (g) | Analytical method |
|----------|--------------------|----------------------|-----------------------------|-----------------------------|-------------------|
| 1 | 340 | 3.5 | 3.10 | 3.28 | 2D-DIC |
| 2 | 340 | 5.5 | 6.43 | 6.68 | 3D-DIC |

area is approximately 394 mm × 289 mm. In addition, the camera shooting parameters for test 2 are as follows. The photograph frame is set as 20000 fps, the image resolution is set as 640 pixels × 536 pixels, and the shooting area is

approximately 356 mm × 298 mm. For test 1 and test 2, the calculated area of interest (AOI) range on the surface of one bevel is approximately 260 mm × 280 mm (Figure 3(a)), the reference subset of pixels in the DIC computation is chosen

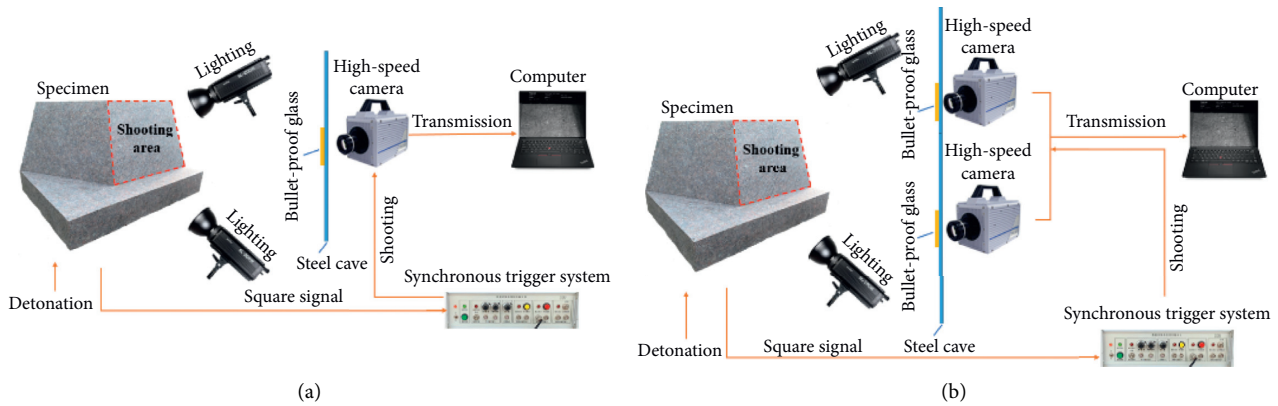


FIGURE 2: Schematic diagram of test systems: (a) test 1 (2D-DIC experimental system); (b) test 2 (3D-DIC experimental system).

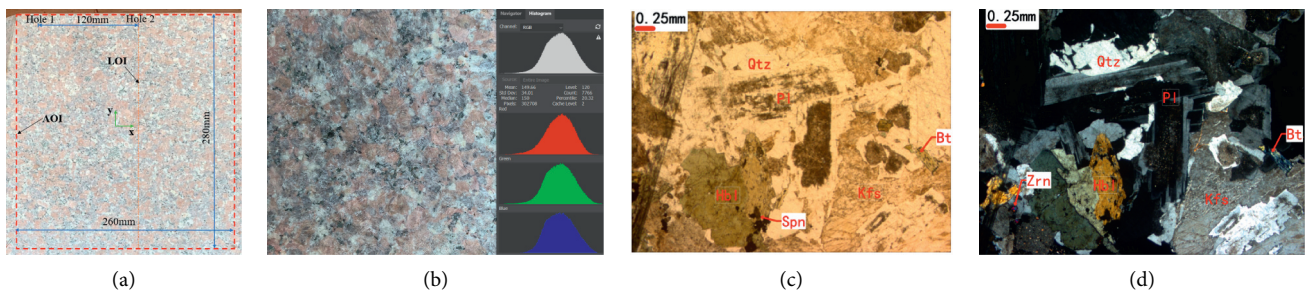


FIGURE 3: Granite specimen. (a) Area of interest for test 1 and test 2; (b) gray value; (c) plane-polarized light; (d) cross-polarized light.

to be $47 \text{ pixels} \times 47 \text{ pixels}$, and a subset step of 7 pixels is used. The average gray value in terms of the current granite specimen is 149.66 (Figure 3(b)). Polarizing microscope images (LEICA DM2500 p) are done in Yunenng geological service (Langfang, China), as shown in Figures 3(c) and 3(d), and the test parameter is 10×2.5 (eyepiece multiple \times objective multiple). The main minerals of the rock are plagioclase (Pl; the main grain size is 2–5 mm, some grain size is 0.5–2 mm.), potassium feldspar (Kfs; the main grain size is 2–5 mm, and some grain size is 5–10 mm.), and quartz (Qtz; the main grain size is 2–5 mm, and some grain size is 0.5–2 mm.), while the secondary minerals are biotite (Bt; the main grain size is 0.2–2 mm.) and amphibole (Hbl; the main grain size is 0.5–2 mm.).

3. Results

3.1. DIC Analysis. The interval between the images is $50 \mu\text{s}$ for test 1 and test 2. The evolution of von Mises strain for the eight frames ($50 \mu\text{s}$, $100 \mu\text{s}$, $150 \mu\text{s}$, $200 \mu\text{s}$, $250 \mu\text{s}$, $300 \mu\text{s}$, $350 \mu\text{s}$, and $400 \mu\text{s}$) is analyzed by VIC-2D analysis software for test 1 (Figure 4), and the evolution of Von Mises strain for the nine frames ($50 \mu\text{s}$, $100 \mu\text{s}$, $150 \mu\text{s}$, $200 \mu\text{s}$, $250 \mu\text{s}$, $300 \mu\text{s}$, $350 \mu\text{s}$, and $400 \mu\text{s}$, and $450 \mu\text{s}$) is analyzed by VIC-3D analysis software for test 2 (Figure 5). If the high-speed photographic images at $0 \mu\text{s}$ and $50 \mu\text{s}$ in test 1 and test 2 are treated as similar to static correction images, it can be found that the Von Mises strain is all approximately smaller than $100 \mu\epsilon$ in the main region, the principal strain has the same

characteristics, and then it can be concluded that the DIC measurement in this paper is effective and accurate [11].

The horizontal distance from the top of the charge to the free surface is approximately 96.4 mm, and the distance from the top of the charge to the vertex position of the two free surfaces to the working place is approximately 121.6 mm; in other words, the time for the stress wave to travel to these two positions is $22 \mu\text{s}$ and $27.7 \mu\text{s}$, respectively. Comparing Figures 4 and 5, the following can be observed: (1) at $300 \mu\text{s}$, one horizontal strain concentration zone locates approximately on the middle of the AOI in both specimens; (2) at $200 \mu\text{s}$ to $350 \mu\text{s}$ of test 1, there is one vertical strain concentration zone, and it changes from the middle of the observed AOI to the whole AOI, and then to the upper part of the horizontal strain concentration zone; (3) from $200 \mu\text{s}$ to $350 \mu\text{s}$ for test 2, there are two vertical strain concentration zones; (4) from $50 \mu\text{s}$ to $200 \mu\text{s}$ for test 1, there is a corner strain concentration zone near the vertex position of two free surfaces on the working place; (5) at $150 \mu\text{s}$ for test 2, there is a corner strain concentration zone near the vertex position of two free surfaces on the working place.

According to the results of full-field strain from 2D-DIC and 3D-DIC analysis, the main potential failure regions in the AOI of the specimen bevel surface can be estimated. The strains are mainly uniaxial tension at different positions, and the difference of the strain field between the two specimens is caused by the different weight of charge. The results show that the increase of charge weight mainly affects the number of the vertical strain concentration area rather than the

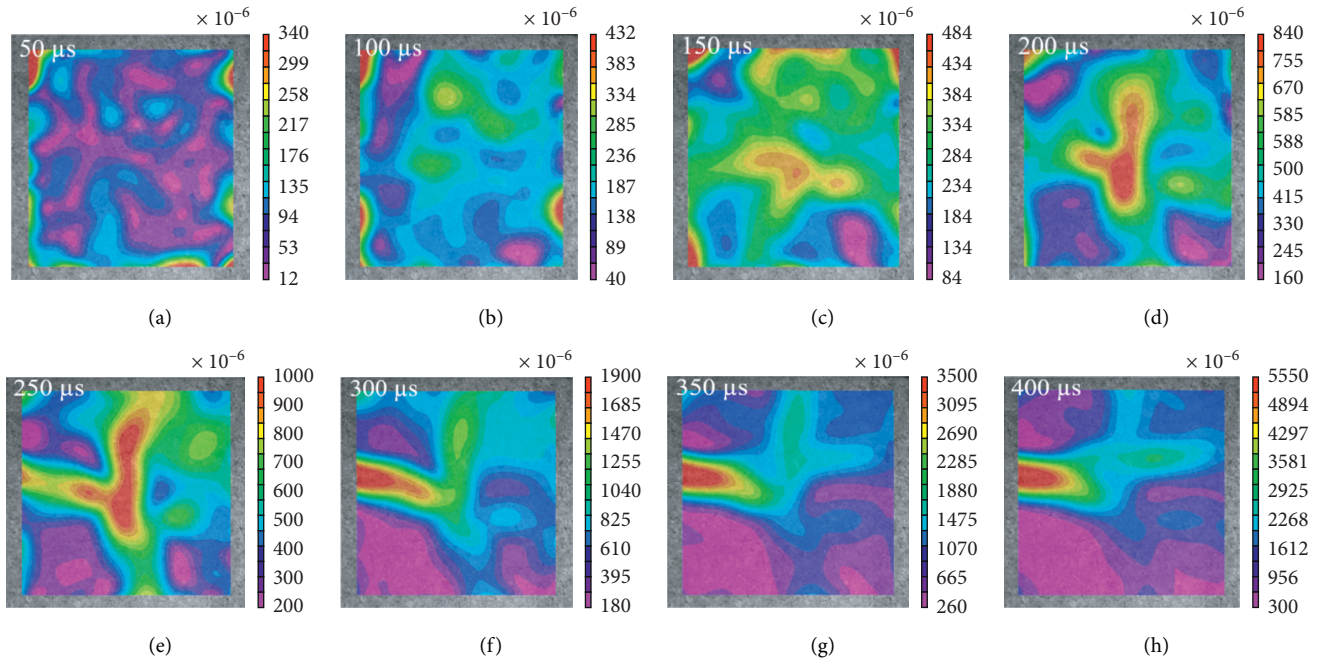


FIGURE 4: The evolution of von Mises strain for test 1. (a) $50 \mu\text{s}$. (b) $100 \mu\text{s}$. (c) $150 \mu\text{s}$. (d) $200 \mu\text{s}$. (e) $250 \mu\text{s}$. (f) $300 \mu\text{s}$. (g) $350 \mu\text{s}$. (h) $400 \mu\text{s}$.

horizontal strain concentration area and affects the vertical direction and location of the vertical strain concentration area.

3.2. Fracture Process. By observing the high-speed photographic images for test 1 in Figure 6, the displacement is visible to the naked eye at $300 \mu\text{s}$ when playing images dynamically, but there is no visible initiation crack; the dominant horizontal initiation crack and crack initiation position can be identified until $350 \mu\text{s}$. As a matter of fact, the crack is formed between $250 \mu\text{s}$ and $300 \mu\text{s}$. The average upward migration of this crack is approximately 33.5° between $350 \mu\text{s}$ and $400 \mu\text{s}$; with time, this crack called the dominant horizontal crack continues to propagate, and it propagates across the entire AOI at $600 \mu\text{s}$. Combined with 2D-DIC analysis data of the dominant horizontal crack initiation position at $250 \mu\text{s}$ and $300 \mu\text{s}$, the principal strain concentration zone and the vertical strain concentration zone locate on the dominant horizontal crack initiation position; the principal strain (ϵ_1) values are 0.0021 and 0.00402 (Figure 7(a)), the Von Mises strain are 0.00095 and 0.0019 (Figure 4), and the strains in the vertical direction (ϵ_{yy}) are 0.00192 and 0.00405 (Figure 7(b)), and it may be considered that the dominant horizontal crack is the tensile crack. The branching crack (yellow arrow in Figure 6) that initiated at the front end of the upward deflection point of the dominant horizontal crack deflects downward by 20.5° and is visible at $550 \mu\text{s}$; at the same time, a crack (mazarine arrow in Figure 6) coming from outside the observation area converges to the dominant horizontal crack after $100 \mu\text{s}$ (ellipse G in Figure 6). It can be seen that there is a shear strain concentration zone located on the branching crack and a shear strain concentration zone located on the crack

coming from outside the observation area in Figure 7(d), and the two cracks may be considered as the shear cracks. However, the branching crack has no contribution to the final fragmentation as shown in Figure 8(c). The first vertical dominant crack is visible at $600 \mu\text{s}$ (ellipse A in Figure 6) and the second vertical dominant crack is visible at $700 \mu\text{s}$ (ellipse B in Figure 6); the axial strain concentration zones locate correspondingly on the two vertical dominant cracks in Figure 7(c). Comparing the two images in Figure 7(c), and the crack formation occurs before visibility, it can be described that the axial strain value is between 0.00275 and 0.0028 because the maximum value of the axial strain locates on the second vertical dominant crack in the time that follows. If so, the first vertical dominant crack may initiate at $500 \mu\text{s}$ and the second vertical dominant crack may initiate at $550 \mu\text{s}$, or they all may initiate at $550 \mu\text{s}$. The second vertical dominant crack has another characteristic that it is converged by two pieces of vertical cracks ($800 \mu\text{s}$ in Figure 6). The first and second vertical dominant cracks converge to the dominant horizontal crack ultimately, and they may be considered as the tensile cracks. And the second vertical dominant crack did not contribute to the formation of fragment during blasting process. It may generate two pieces of blocks as the fragment falls to the ground.

By observing the high-speed photographic images for test 2 in Figure 9, the displacement is visible to the naked eye at $200 \mu\text{s}$ when playing images dynamically, but there is no visible initiation crack. The dominant horizontal initiation crack and crack initiation position can be identified until $250 \mu\text{s}$. As a matter of fact, the crack is formed between $150 \mu\text{s}$ and $200 \mu\text{s}$. Combined with 3D-DIC analysis data of the dominant horizontal crack initiation position at $150 \mu\text{s}$ and $200 \mu\text{s}$, the principal strain values are 0.00128 and 0.00308 (Figure 10(a)). The Von Mises strains are 0.000634

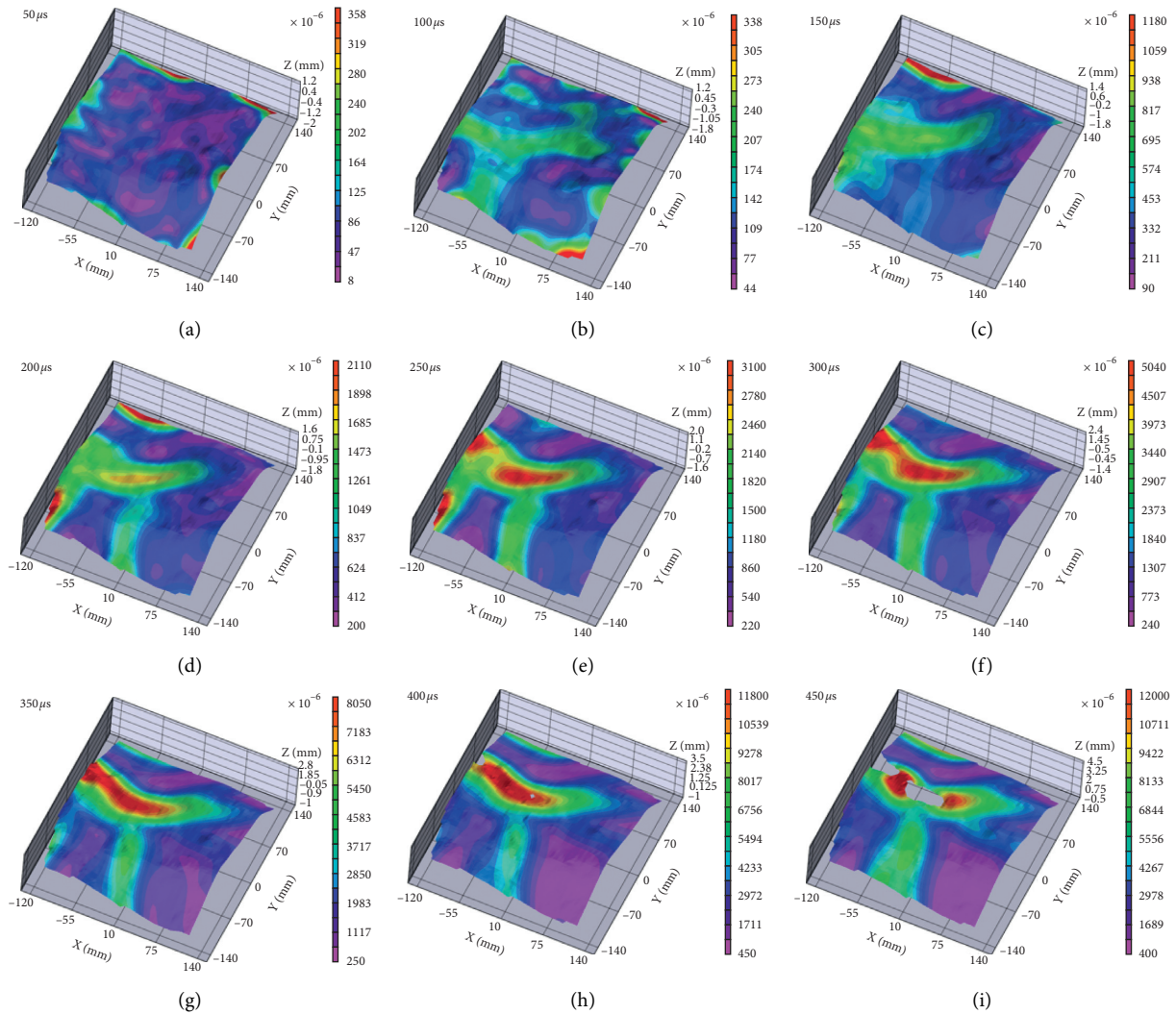


FIGURE 5: The evolution of von Mises strain for test 2. (a) $50 \mu s$. (b) $100 \mu s$. (c) $150 \mu s$. (d) $200 \mu s$. (e) $250 \mu s$. (f) $300 \mu s$. (g) $350 \mu s$. (h) $400 \mu s$. (i) $450 \mu s$.

and 0.001579 (Figure 5), and the strains in the vertical direction (ϵ_{yy}) are 0.00133 and 0.00286 (Figure 10(b)). The dominant horizontal crack coming from crack initiation point propagates downward in three segments by 56° , 9.5° , and 37° , respectively, and then it propagates upward by 20.5° . The dominant horizontal crack propagates across the entire AOI at $500 \mu s$, and there is a dislocation crack in the front of the dominant horizontal crack at $350 \mu s$; it can be clearly seen at $400 \mu s$ that there is a distance between the two cracks on the surface of the specimen (yellow arrow and red arrow in Figure 7). In addition, a crack, which has a distance with the dominant horizontal crack on the surface of the specimen, is generated near the dislocation position by 68° at $450 \mu s$ (green arrow in Figure 7). It is difficult to determine whether it is a branching crack, and the three cracks interpenetrate at $700 \mu s$ from observing the surface of the specimen, and the branching crack is observed at $700 \mu s$ and the angle between the branching crack and the dominant horizontal crack is 72.5° (Ellipse I in Figure 7). Uncertain branching crack and branching crack have axial strain

concentration zones as shown in Figure 10(c) by $450 \mu s$ and $600 \mu s$, and they may be considered as the tensile cracks. The first vertical dominant crack is visible at $400 \mu s$ (ellipse C in Figure 7) and it is converged by three pieces of vertical cracks ($600 \mu s$ in Figure 6); the second and third vertical dominant cracks are visible at $450 \mu s$ (ellipse D and ellipse E in Figure 7) and they have approximately the same crack initiation direction of propagation (37° and 38° , respectively), and the fourth vertical dominant crack is visible at $500 \mu s$ (ellipse H in Figure 7). The axial strain value is between 0.00232 and 0.0028 using the same analysis method in test 1. In addition, there is a crack visible at $400 \mu s$; then, it presents crack closure, and it is observed again to be at $4000 \mu s$ and this crack contributes to the formation of a fragment (ellipse F in Figure 7). And the first vertical dominant crack travels through the end of the crack F and converges to the dominant horizontal crack ultimately.

The fracture process of simultaneous rock blasting under different charge weights based on a double-hole bench model has the following characteristics: (1) the dominant

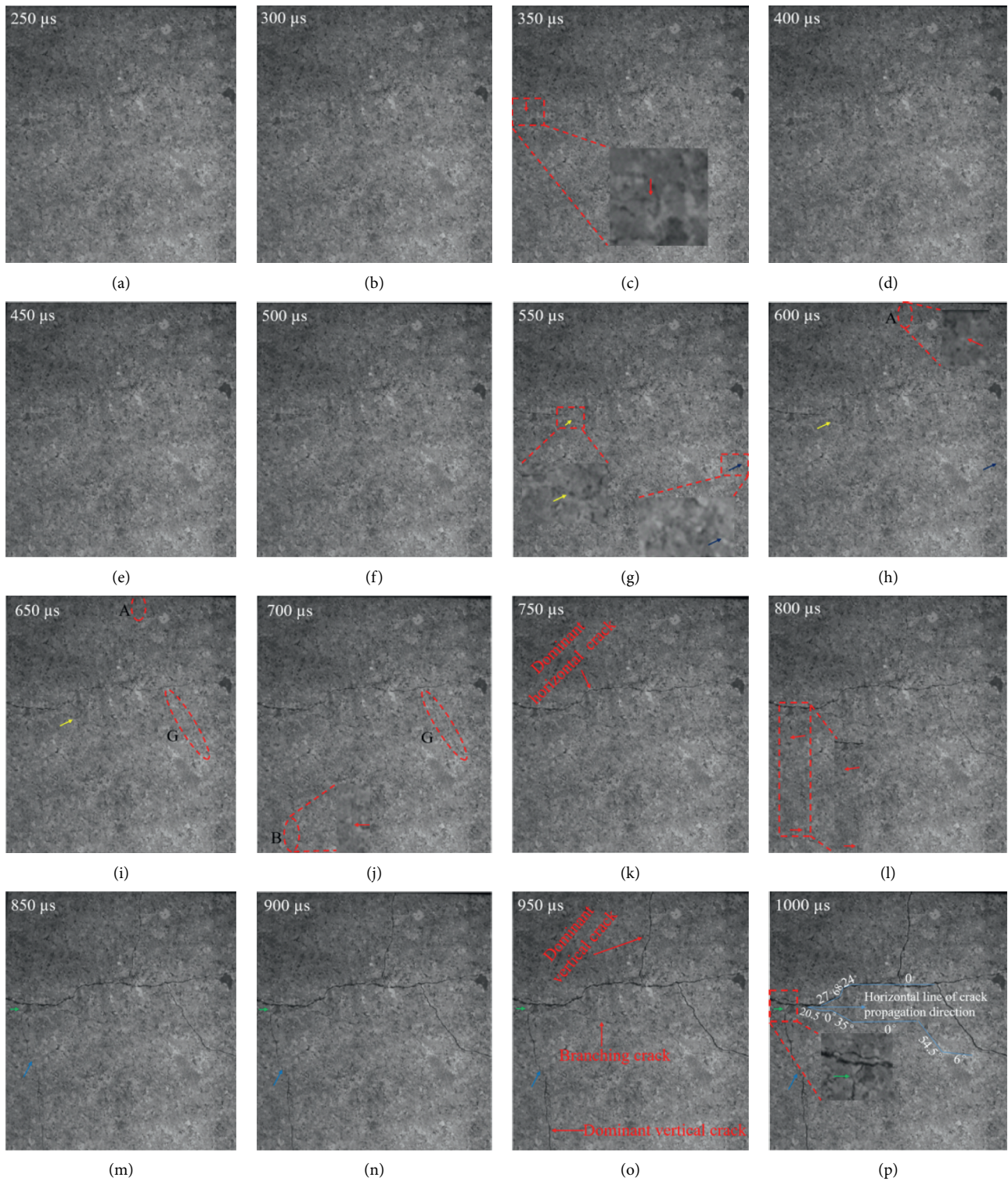


FIGURE 6: The crack evolution for test 1 (the magnification of the enlarged part is 300%). (a) 250 μ s. (b) 300 μ s. (c) 350 μ s. (d) 400 μ s. (e) 450 μ s. (f) 500 μ s. (g) 550 μ s. (h) 600 μ s. (i) 650 μ s. (j) 700 μ s. (k) 750 μ s. (l) 800 μ s. (m) 850 μ s. (n) 900 μ s. (o) 950 μ s. (p) 1000 μ s.

horizontal crack, which locates approximately on the middle of the AOI in both specimens, initiates at the junction of the two free surfaces; it expands horizontally with time increases; the growth of the horizontal crack is accompanied by the generation of the branch cracks in the process; (2) the

dominant vertical cracks initiate at the interface between working face and free surface and between the bottom platform and free surface; the dominant vertical cracks initiated between the bottom platform and free surface are converged by two or three pieces of vertical cracks; (3) the

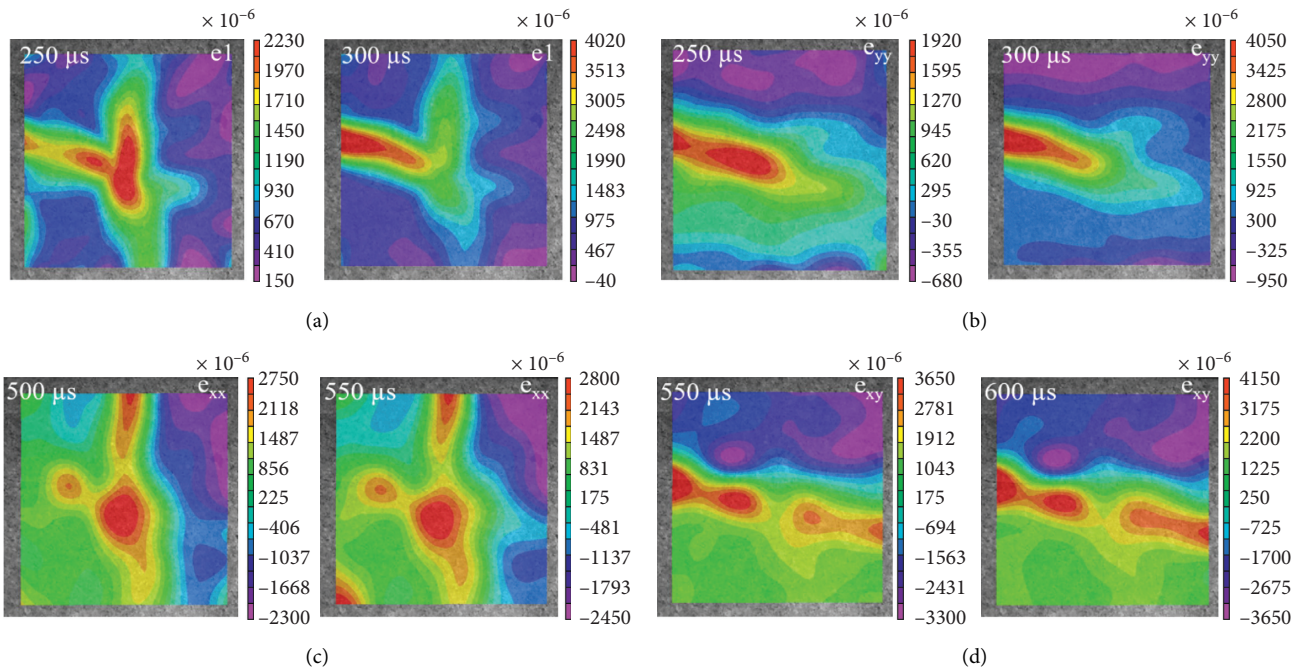
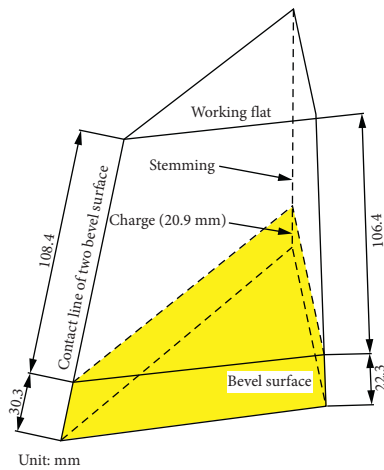
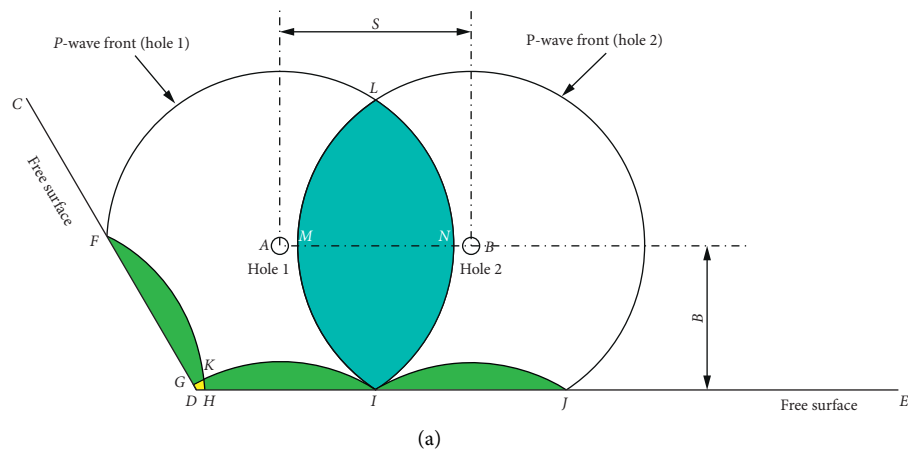


FIGURE 7: Full-field strain characterizations of crack initiation for test 1: (a) e_1 ; (b) e_{yy} ; (c) e_{xx} ; (d) e_{xy} .



(b)

(c)

FIGURE 8: Stress wave distribution and the first crack initiation on the bevel surface in the simultaneous rock blasting: (a) stress wave distribution; (b) a part of double-hole bench model; (c) a part of fragmentation for test 1.

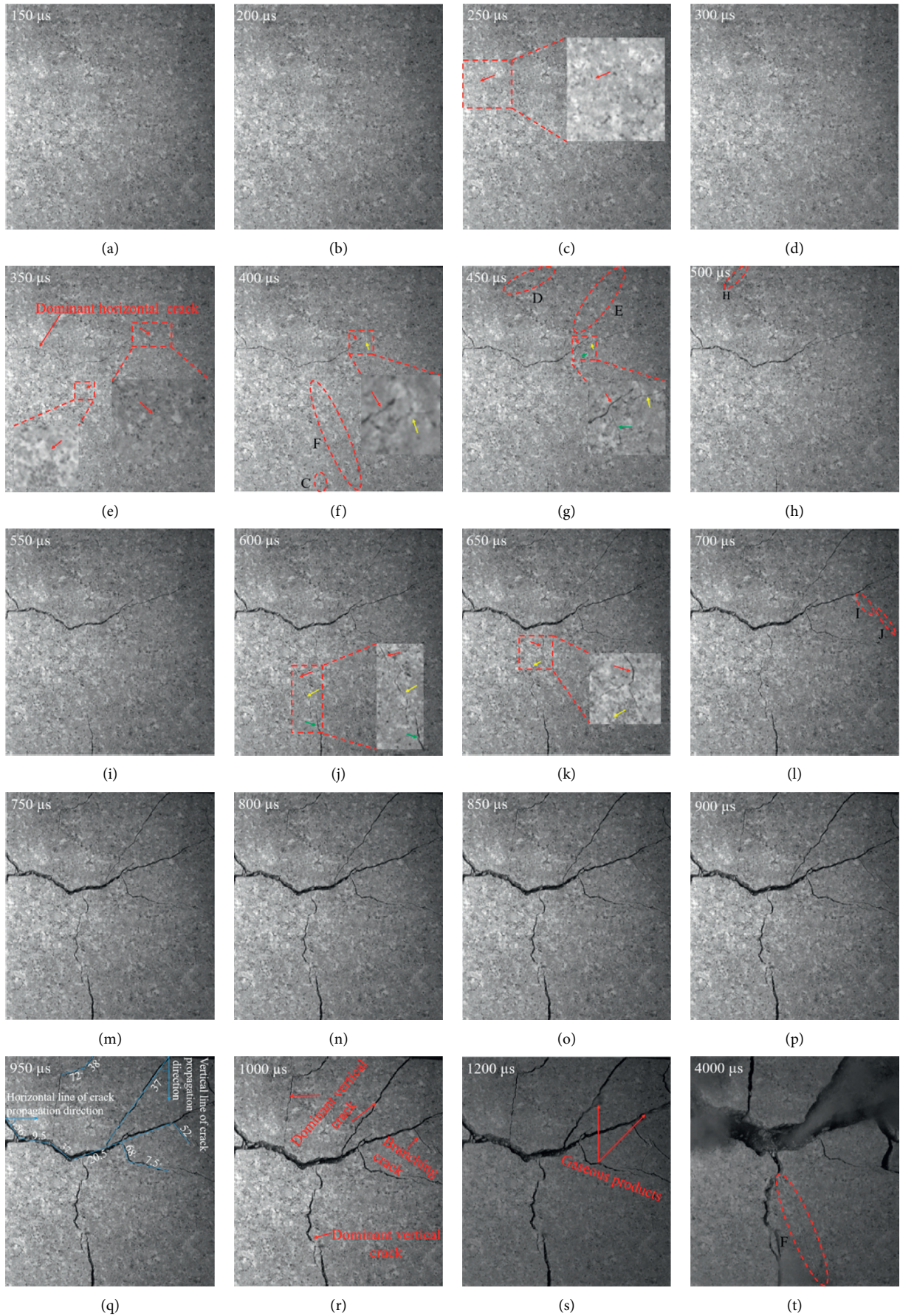


FIGURE 9: The crack evolution for test 2 (the magnification of the enlarged part is 300%). (a) 150 μs . (b) 200 μs . (c) 250 μs . (d) 300 μs . (e) 350 μs . (f) 400 μs . (g) 450 μs . (h) 500 μs . (i) 550 μs . (j) 600 μs . (k) 650 μs . (l) 700 μs . (m) 750 μs . (n) 800 μs . (o) 850 μs . (p) 900 μs . (q) 950 μs . (r) 1000 μs . (s) 1200 μs . (t) 4000 μs .

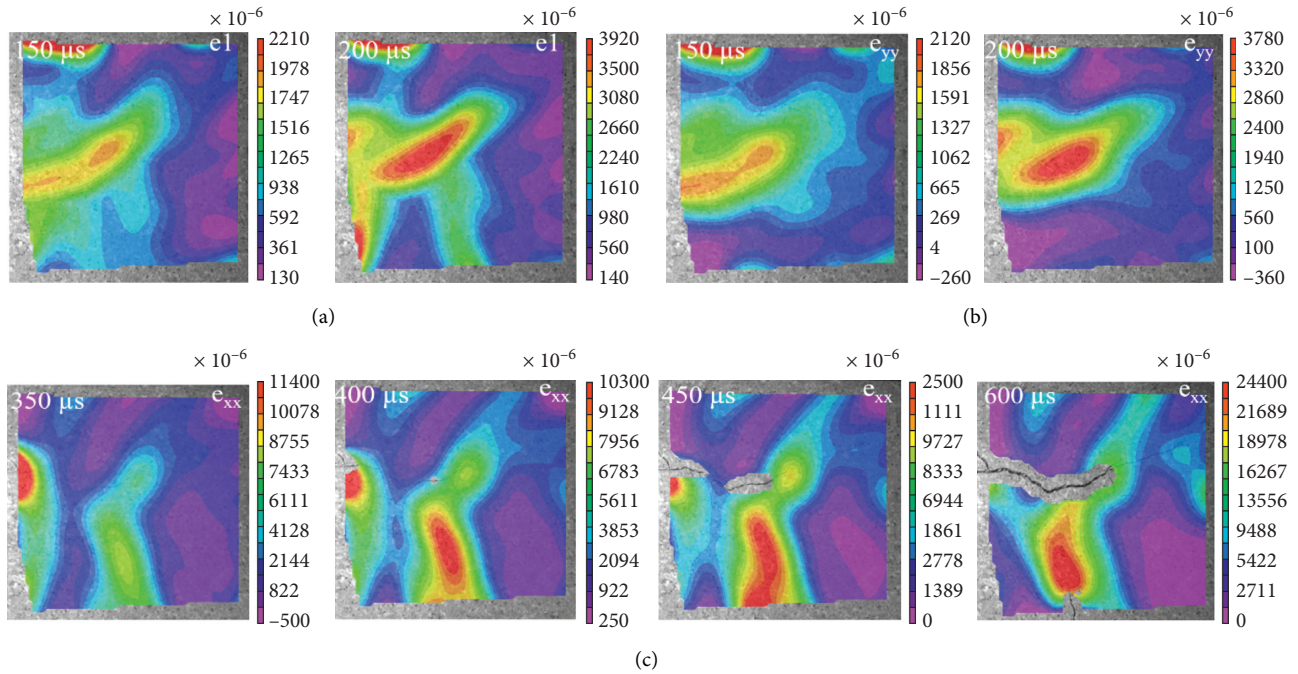


FIGURE 10: Full-field strain characterizations of crack initiation for test 2: (a) e_1 ; (b) e_{yy} ; (c) e_{xx} .

dominant horizontal crack propagates preferentially than that of dominant vertical crack, and the dominant horizontal crack opening angle is greater than that of the dominant vertical crack. The crack initiation time, the number of cracks, and the crack opening angle are effected by charge weight. Evidence of the statement of Bhandari [3] can be found. According to the research of Bhandari [2], it is reasonable to assume that the larger strain-energy-density supply leads to the very high velocity of the cracks, the number of dominant vertical cracks and bifurcations under large charge weight conditions. The more dominant vertical cracks and bifurcations, the smaller the fragment size. At critical charge weight, perhaps the strain-energy-density is just sufficient to propagate a dominant horizontal crack at low velocity. Therefore, no dominant vertical cracks and bifurcations generate. Similarly, larger fragments are produced at a charge weight smaller than the critical; (4) Erdogan and Sih [13] concluded that the crack growth direction is perpendicular to the maximum tension. By combining Figures 7 and 10, the distribution of the strain fields in the vertical direction is related to the horizontal crack propagation direction, and it can be concluded that the dominant horizontal crack and the dominant vertical crack are tensile cracks.

4. Discussion

4.1. The First Crack on the Bevel Surface. The stress and fracture interactions between blast holes actually occur in three dimensions, so these interactions should be analyzed in three dimensions. Alternatively, the interactions can be analyzed along the borehole axis section or in cross section of borehole [14]. In order to simplify the analysis, the

analysis is limited to the cross section of the borehole. As shown in Figure 8(a), we assume that the spacing S is 120 mm, boundary CD and DE are free surface, and the angle of boundary CDE is 120° . According to the literature [14], it can be described as follows. Only P-waves are considered in each hole, while S-waves are ignored. Once the charges in the holes are simultaneously initiated, P-waves begins to propagate outward. After a while, the front of the P-waves reaches the position where the two circles are located in the area surrounded by $FLJIHKF$. Overlap area $LMINL$ exists in this region. During this period time, three tensile stress waves enter the model from the free surface CD and DE . There are located in the area $FKHDGF$, $GKIHDG$, and IJI . For the moment, we are interested in the overlap area $GKHD$, which emerges earlier than the overlap area from area $GKIHDG$ and IJI . Similar cases similar to Figure 8(a) happen in the cross section of the borehole when the burden B is in the range between 96.4 mm and 104 mm. In other words, the location is between the top of charge and extending down 20.9 mm. Taking the working flat as the datum plane, the distance corresponding to the bevel surface is between 106.4 mm and 128.7 mm; the distance corresponding to the contact line of two bevel surfaces is between 108.4 mm and 138.7 mm, as shown in Figure 8(b).

In addition, first, a new fracture surface long line AB will be established very quickly due to tangential stress, and much energy will be concentrated on it. Thus other radial cracks may slow down [14]. Second, Fournery [15] summarized that the most intense crack initiation mechanism is the combined action of PP-wave and PS-wave near the free surface. This mechanism is not necessarily the most important for overall fragmentation, but it has been shown to cause defects near the free surface at great distances from the

borehole. As the reflected P-wave components return further into the medium, they encounter the outgoing S-wave. The phase length interference between the two types of wave systems resulted in two different crack initiation zones. Defects in these areas are most likely to be initiated. Third, the stress wave decays as the distance increases. Tensile fracturing will only occur if the wave amplitude has exceeded a certain threshold [16]. Fourth, based on an example of linear elastic fracture mechanics, Exadaktylos [17] demonstrated that a crack close to more than one free surface has a higher stress intensity than a crack close to one free surface with the same internal pressure. Fifth, for test 2, the distance between the top of charge and contact line of bevel surface in the cross section of the borehole is 104.7 mm, explosive detonation complete time is $340 \text{ mm}/5200 \text{ m}\cdot\text{s}^{-1} = 65.4 \mu\text{s}$, and the crack initiation time is $150 \mu\text{s}$ based on the visible method. Thus the velocity of crack that is propagated from the borehole is $104.7 \text{ mm}/(150 \mu\text{s} - 65.4 \mu\text{s}) = 1237.6 \text{ m}\cdot\text{s}^{-1}$. The crack propagation velocity measured from SHPB (split Hopkinson pressure bar) experiments of L-granite rock is between 300 and $850 \text{ m}\cdot\text{s}^{-1}$ [18]. Sixth, the angle between the contact line of the bevel surface and borehole is 29.5° . According to Table 1, it is easy to compute the velocity of S-wave ($2444 \text{ m}\cdot\text{s}^{-1}$), and thus Mach angle of the P-wave and S-wave is shown in Table 3. Therefore, it can be seen that the front of the S-wave is approximately parallel to the contact line of the bevel surface. Fournery et al. [20] designed the tests to make the wave front of the P-wave parallel to the boundary. They found that spacing of the line charge relative to the vertical boundary should not markedly affect the vertical positioning of the region where spallation occurs but influence the extended amounts of the spallation. Rossmanith et al. [21] demonstrated that the superposition of S-Mach wave and SP-wave generates high shear stress to easily make a crack initiation or promote the extension of a fracture. Seventh, the gaseous products did not escape when the first crack initiates on the bevel surface.

In conclusion, it can be found that the stress wave distribution and the first crack initiation on the bevel surface in the simultaneous rock blasting have the following implied characteristics: (1) the first crack observed on the bevel surface did not initiate from the borehole; (2) S-Mach wave and SP-wave may promote the extension of a fracture near the contact line of two bevel surfaces; (3) the singularity effects near the horizontal crack tips are more effective than those of the vertical cracks; (4) stress waves reflected from the work platform also promote the extension of the first crack observed on the bevel surface, as shown in Figures 7(b) and 10(b).

4.2. Comparison of 3D-DIC and 2D-DIC for Test 2. Figure 7 ($4000 \mu\text{s}$) and Figure 5 show a degree of elevation in the Z-direction; e.g., the maximum value in the Z-direction is from 1.6 mm ($200 \mu\text{s}$) to 4.5 mm ($450 \mu\text{s}$). In other words, the bevel surface exists out-of-plane motions, which may affect the measurement of the object deformation. To match the relationship between high-speed camera images and DIC analysis, the same images in the main camera are used

to process the 2D-DIC with the same parameters setting as the 3D-DIC. Six types of strain at the same position of the line of interest (LOI) (Figure 3), which locates on the surface of the bevel in the vertical direction of Hole 2, are discussed. Based on the comparison in Figure 11, the trend of the curve pattern is basically the same between 3D-DIC and 2D-DIC analysis for six types of strain. Although the numerical deviation of the peak point is not large, the position deviation of the maximum point is relatively large. By comparing the peak point data between 2D-DIC and 3D-DIC analysis on six types of strain (if there are multiple positions for the same peak point, we treat it as an average), the results are as follows: (1) for 3D-DIC and 2D-DIC analysis on e_{xx} , the coordinate points of the peak point are $-11.35, 0.00168$ and $-16.44, 0.00148$, respectively. The relative difference value in both is $5.09, 0.0002$; (2) from 3D-DIC and 2D-DIC analysis on e_{yy} , the coordinate points of the peak point are $3.97, 0.00348$ and $0.14, 0.00321$, respectively; the relative difference value in both is $3.83, 0.00027$; (3) from 3D-DIC and 2D-DIC analysis on e_{xy} , the coordinate points of the peak point are $16.75, -0.00108$ and $28.26, -0.00166$, respectively; the relative difference value in both is $-11.51, 0.00058$; (4) from 3D-DIC and 2D-DIC analysis on e_1 , the coordinate points of the peak point are $10.36, 0.00384$ and $12.91, 0.00375$, respectively; the relative difference value in both is $-2.55, 0.00009$; (5) from 3D-DIC and 2D-DIC analysis on e_2 , the coordinate points of the peak point are $-22.79, 0.00171$ and $17.71, 0.00147$, respectively; the relative difference value in both is $40.5, 0.00024$; (6) from 3D-DIC and 2D-DIC analysis on von Mises strain, the coordinate points of the peak point are $9.08, 0.00173$ and $18.03, 0.00182$, respectively; the relative difference value in both is $-8.95, -0.00009$. For the sample size of this experiment, we can find that the principal strain (e_1) can be accepted in both 3D-DIC and 2D-DIC analysis from the above simple description.

A measurement point, which locates approximately 4 mm from the LOI in the positive Y-axis, is selected. Based on the comparison in Figure 12, the trend of the curve pattern is basically the same between 3D-DIC and 2D-DIC analysis for six types of strain from $50 \mu\text{s}$ to $400 \mu\text{s}$. The difference in the time that followed varies greatly. Let us say that we use the data of 3D-DIC as a benchmark and then employ a simple evaluation index, which is the difference value between the data of 3D-DIC and the data of 2D-DIC and then divide by the data of 3D-DIC. Analyzing the six types of strain from $50 \mu\text{s}$ to $400 \mu\text{s}$, the results of the evaluation index are as follows: (1) by analyzing 3D-DIC and 2D-DIC on e_{xx} , the maximum value is 28.21% ($150 \mu\text{s}$), the minimum value is 4.52% ($50 \mu\text{s}$), and the mean value is 14.36% ; (2) by analyzing 3D-DIC and 2D-DIC on e_{yy} , the maximum value is 116.20% ($50 \mu\text{s}$), the minimum value is -2.37% ($250 \mu\text{s}$), and the mean value is 24.48% ; (3) by analyzing 3D-DIC and 2D-DIC on e_{xy} , the maximum value is 81.75% ($50 \mu\text{s}$), the minimum value is -28.47% ($150 \mu\text{s}$), and the mean value is 27.25% ; (4) by analyzing 3D-DIC and 2D-DIC on e_1 , the maximum value is 99.79% ($50 \mu\text{s}$), the minimum value is -3.89% ($250 \mu\text{s}$), and the mean value is 18.01% ; (5) by analyzing 3D-DIC and 2D-DIC on e_2 , the

TABLE 3: Charge parameters.

| Test no. | Average charge density (g/cm^3) | Detonation velocity (m/s) [19] | Mach angle of the P-wave | Mach angle of the S-wave |
|----------|---|--------------------------------|--------------------------|--------------------------|
| Test 1 | 0.97 | 5800 | 49° | 25° |
| Test 2 | 0.82 | 5200 | 58° | 28° |

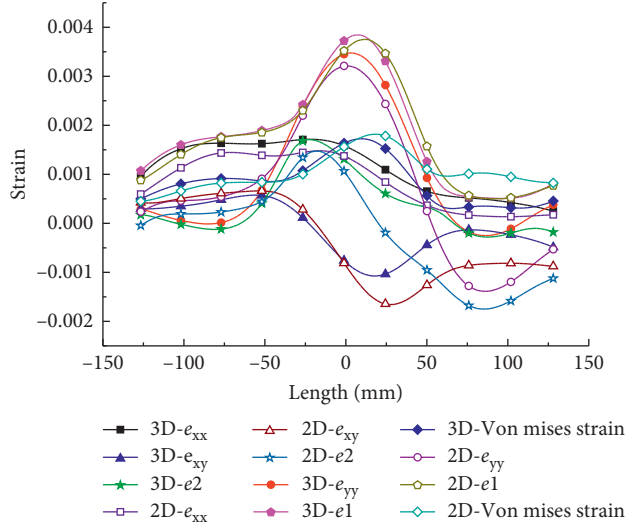
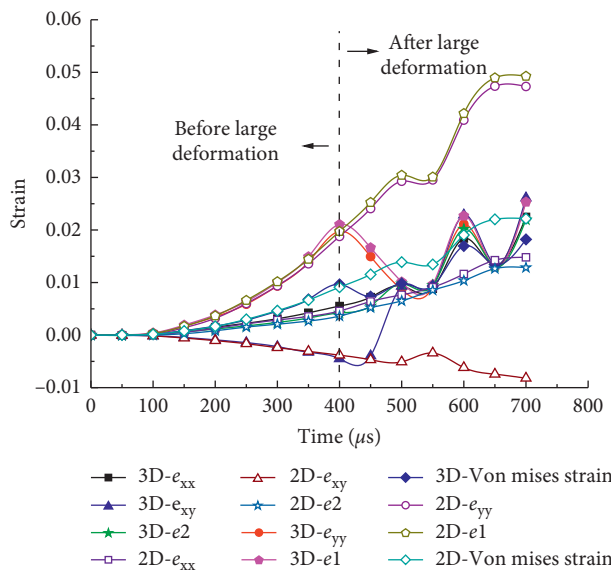
FIGURE 11: Comparison of 3D-DIC and 2D-DIC analysis at $200 \mu\text{s}$ for test 2.

FIGURE 12: Comparison of 3D-DIC and 2D-DIC analysis with time increases for test 2.

maximum value is 105.61% ($100 \mu\text{s}$), the minimum value is 12.96% ($250 \mu\text{s}$), and the mean value is 35.98%; (6) by analyzing 3D-DIC and 2D-DIC on Von Mises strains, the maximum value is 62.27% ($50 \mu\text{s}$), the minimum value is -5.36% ($250 \mu\text{s}$), and the mean value is 10.90%. As time goes on, the difference is clear in both 3D-DIC and 2D-DIC analysis from the above simple description.

On the one hand, 2D-DIC theoretically is restricted to planar surfaces and predominantly in-plane deformations

[11]. This would lead to sensitivity about out-of-plane motion of 2D-DIC; on the other hand, the movement of the bench surface is the outward expansion under blast loading [2]. In other words, the error of the measurements of 2D-DIC is going to get bigger and bigger when a crack is going to open. Based on the principle of binocular stereovision [12], it is worth noting that 3D-DIC is theoretically able to extract precisely the surface deformations in the plane, even when the object is undergoing large, three-dimensional rigid body rotation and translation [11].

5. Conclusions

Field bench blasting is the result of multihole blasting interaction. It makes sense to provide a theoretical basis for such a practical situation. Therefore, a small-scale double-hole bench model is designed with granite to study the full-field strain characterizations and fracture process of rock blasting. The test results show the following: (1) DIC can well provide the main potential failure locations and the fracture strain on the specimen bevel surface. It can be concluded that the distribution of the strain fields in the vertical direction is related to the dominant horizontal crack propagation direction, stress waves reflected from the working platform promotes the extension of the dominant horizontal crack observed on the bevel surface; the dominant horizontal crack and the dominant vertical crack are tensile cracks, and the branching crack is shear crack or tensile crack; (2) through observing the crack propagation pattern on the specimen bevel surface, it can be seen that the fracture of the specimen is mainly caused by the dominant horizontal crack and the dominant vertical crack. Based on the fracture process in simultaneous rock blasting under different charge weights. It is found that the dominant horizontal crack propagates preferentially than the dominant vertical crack, the dominant vertical crack near working platform propagates preferentially than that near bottom platform, and the crack initiation time, the number of cracks, and the crack opening angle are effected by charge weight; (3) through the discussion of the dominant horizontal crack initiation mechanism, it can be concluded that the dominant horizontal crack observed in average charge density of $0.82 \text{ g}/\text{cm}^3$ does not come from radial crack propagation, and this crack initiates on the bevel surface. The singularity effects near the horizontal crack tips are more effective than those of the vertical cracks; (4) through comparing the measurements of time scale and length scale of 2D-DIC and 3D-DIC, it can be seen that the error of the measurements of 2D-DIC is going to get bigger and bigger when a crack is going to open. It is recommended to use 3D-DIC in bench model experiment under blast loading when large deformation needs to be measured.

Data Availability

The data used to support the findings of this study are available from the corresponding author upon request.

Conflicts of Interest

The authors declare that they have no conflicts of interest.

Acknowledgments

The authors gratefully acknowledge the support of the National Science Foundation of China (no. 51774043) and the Science Foundation Program of Liaoning Province (no. 20170540456).

References

- [1] M. Saharan, H. Mitri, and J. Jethwa, "Rock fracturing by explosive energy: review of state-of-the-art," *Fragblast*, vol. 10, no. 1-2, pp. 61-81, 2006.
- [2] S. Bhandari, *Engineering Rock Blasting Operations*, A.A. Balkema, Rotterdam, Netherlands, 1997.
- [3] S. Bhandari, "On the role of stress waves and quasistatic gas pressure in rock fragmentation by blasting," *Acta Astronautica*, vol. 6, no. 4, pp. 365-383, 1979.
- [4] M. Olsson, S. Nie, and I. Bergqvist, "What causes cracks in rock blasting?" *Fragblast*, vol. 6, no. 2, pp. 221-233, 2002.
- [5] M. S. Stagg, "Influence of blast delay time on rock fragmentation: one-tenth scale tests," *International Journal of Surface Mining, Reclamation and Environment*, vol. 1, no. 4, pp. 215-222, 1987.
- [6] D. Johansson and F. Ouchterlony, "Shock wave interactions in rock blasting: the use of Short delays to improve fragmentation in model-scale," *Rock Mechanics and Rock Engineering*, vol. 46, no. 1, pp. 1-18, 2013.
- [7] G. Gao, S. Huang, and K. Xia, "Application of digital image correlation (DIC) in dynamic notched semi-circular bend (NSCB) tests," *Experimental Mechanics*, vol. 55, pp. 95-104, 2015.
- [8] Q. B. Zhang and J. Zhao, "Determination of mechanical properties and full-field strain measurements of rock material under dynamic loads," *International Journal of Rock Mechanics & Mining Sciences*, vol. 60, pp. 423-439, 2013.
- [9] H. Z. Xing, Q. B. Zhang, and D. Ruan, "Full-field measurement and fracture characterisations of rocks under dynamic loads using high-speed three-dimensional digital image correlation," *International Journal of Impact Engineering*, vol. 113, pp. 61-72, 2018.
- [10] C. L. He and J. Yang, "Experimental and numerical investigations of dynamic failure process in rock under blast loading," *Tunnelling and Underground Space Technology*, vol. 83, pp. 552-564, 2019.
- [11] M. A. Sutton, H. W. Schreier, and J. J. Orteu, *Image Correlation for Shape, Motion and Deformation Measurements: Basic Concepts, Theory and Applications*, Springer, Berlin, Germany, 2009.
- [12] P. F. Luo, Y. J. Chao, and M. A. Sutton, "Accurate measurement of three-dimensional deformation in deformable and rigid bodies using computer vision," *Experimental Mechanics*, vol. 33, no. 2, pp. 123-132, 1993.
- [13] F. Erdogan and G. C. Sih, "On the crack extension in plates under plane loading and transverse shear," *Journal of Basic Engineering Transactions ASME*, vol. 85, pp. 519-525, 1963.
- [14] Z. X. Zhang, *Rock Fracture and Blasting: Theory and Applications*, Butterworth-Heinemann, Oxford, UK, 2016.
- [15] W. L. Fourny, "The role of stress waves and fracture mechanics in fragmentation," *Blasting Fragment*, vol. 9, pp. 83-106, 2015.
- [16] H. P. Rossmannith, "The use of Lagrange diagrams in precise initiation blasting. Part I: two interacting blastholes," *Fragblast*, vol. 6, no. 1, pp. 104-136, 2002.
- [17] G. E. Exadaktylos, "Computer Aided Blast Fragmentation Prediction," *Virginia Polytechnic Institute and State University*, Commonwealth of Virginia, Blacksburg, VA, USA, 1988.
- [18] Q. B. Zhang and J. Zhao, "A review of dynamic experimental techniques and mechanical behaviour of rock materials," *Rock Mechanics and Rock Engineering*, vol. 47, no. 4, pp. 1411-1478, 2014.
- [19] Y. H. Zhao, S. Q. Duan, H. F. Liu, and G. M. Zhang, "Equation of state of detonation products for RDX explosive," *Chinese Journal of High Pressure Physics*, vol. 29, no. 1, pp. 47-51, 2015.
- [20] W. L. Fourny, J. W. Dally, and D. C. Hollowly, "Stress wave propagation from inclined line charges near a bench face," *International Journal of Rock Mechanics & Mining Sciences & Geomechanics Abstracts*, vol. 11, no. 10, pp. 393-401, 1974.
- [21] H. P. Rossmannith, K. Uenishi, and N. Kouzniak, "Blast wave propagation in rock mass—Part I: monolithic medium," *Fragblast*, vol. 1, no. 3, pp. 317-359, 1997.